PCCP

Accepted Manuscript

ROYAL SOCIETY OF CHEMISTRY

www.rsc.org/pccp

High thermal sensitivity and selectable upconversion color of Ln, Yb:$Y_6O_5F_8$ nanotubes

Carlos Zaldo and Concepción Cascales*

Instituto de Ciencia de Materiales de Madrid, Consejo Superior de Investigaciones Científicas.

c/ Sor Juana Inés de la Cruz 3, E-28049 Madrid, Spain. *ccascales@icmm.csic.es

Yb^{3+}-sensitized, Ln^{3+}(Er^{3+}, Pr^{3+})-doped $Y_6O_5F_8$ micron-sized bundles of highly crystalline individual nanotubes have been prepared through hydrothermal syntheses at 185 ºC. The inhomogeneous broadening observed in their optical spectra is associated to the large distribution of crystal fields around Y^{3+}(Ln^{3+}) sites in the orthorhombic *Pbcm* Vernier-type $Y_6O_5F_8$ host. Based on ratiometric analyses of the thermal evolution of intensities of near-infrared NIR (~978 nm)-excited green upconversion emissions corresponding to $^2H_{11/2}$, $^4S_{3/2}\rightarrow{}^4I_{15/2}$ Er^{3+} transition, the temperature sensing behaviour of Er, Yb:$Y_6O_5F_8$ was studied. This thermal sensor exhibits a very high sensitivity S = 0.0060 K^{-1} at physiological temperatures, that surpasses the S value found for Er, Yb:β-$NaYF_4$ at these temperatures, and a maximum S = 0.0082 K^{-1} at ~ 500 K. Also under NIR diode laser excitation, the color of the upconverted light from codoped Pr, Er, Yb:$Y_6O_5F_8$ nanotubes can be selected by the control of the Pr^{3+} concentration and by the excitation regime and power density. Samples with low Pr^{3+} concentration emit green light, and the selection between bluish-green light and white light has been demonstrated with large Pr^{3+} concentration (2 mol%), under pulsed or continuous wave excitation, respectively.

1 Introduction

Research in inorganic optically active trivalent lanthanide (Ln)-based upconverting particles (Ln-UCPs) is nowadays stimulated by their successful exploitation in two main fields of photonics applications. The first is the development of ultrasensitive markers to be used in security technology,[1] and in a range of imaging and sensing techniques, which includes operation as selective biological probes[2,3,4] and thermal sensing at the sub-micrometric scale, in particular as accurate cellular thermometers.[5,6,7,8,9] Benefits of Ln-UCPs as biolabels derive from the use of inexpensive near infrared (NIR) diode lasers (DL) as efficient excitation sources, the compatibility of excitation wavelengths with the tissue penetration window (700-1000 nm), that makes possible deep penetration without damaging the analyzed specimen, as well as the absence of autofluorescent background signals, leading to the enhancement in resolution imaging. Furthermore, for non-invasive optical temperature sensing, current developments with Ln-UCPs are often carried out by applying the fluorescence intensity ratio method.[10,11] For this purpose, green emissions from Er^{3+} corresponding to electronic transitions $^2H_{11/2}\rightarrow{}^4I_{15/2}$ (at ~ 530 nm) and $^4S_{3/2}\rightarrow{}^4I_{15/2}$ of Er^{3+} (at ~ 550 nm) are particularly appropriate,[6,7,9,12] and Yb^{3+} is the usual sensitizer of Er^{3+} upconversion processes.

The second field of photonic applications of Ln-UCPs deals with lighting technologies, namely the fabrication of color displays and devices,[13] and the development of white light sources. Generation of white light from Ln-UCPs can be achieved by the balance of the intensity of upconverted red, green and blue (RGB) lights, which is usually reached by co-doping a same crystalline host with two or more different active Ln^{3+} along with the presence of Yb^{3+} as sensitizer. Among the explored combinations of Ln^{3+} the most popular ones are: i) (Yb), Er, Tm,[4,14,15,16,17] that provides emissions at ~645-670 nm (red, $^4F_{9/2}\rightarrow{}^4I_{15/2}$ Er^{3+} transition), ~520-565 nm (green, $^2H_{11/2}$,$^4S_{3/2}\rightarrow{}^4I_{15/2}$ Er^{3+} transitions) and ~450-490 nm (blue, $^1D_2\rightarrow{}^3F_4$ and $^1G_4\rightarrow{}^3H_6$ Tm^{3+} transitions); ii) (Yb), Ho, Tm,[4,18,19,20] with main visible emissions at ~645-665 nm (red, $^5F_5\rightarrow{}^5I_8$ Ho^{3+} transition), 545-565 nm (green, $^5F_4$,$^5S_2\rightarrow{}^5I_8$ Ho^{3+} transitions) and ~475 nm (blue, $^1G_4\rightarrow{}^3H_6$ Tm^{3+} transition); and iii) (Yb), Ho, Tm, Er combination, that has been successfully tested in nanocrystalline silica-coated $GdVO_4$.[21] As an alternative, Yb^{3+}-sensitized Pr^{3+} systems offer the possibility of simultaneous blue (~485 nm), green (~525 nm) and red (~640 nm) upconverted emissions, and additionally also orange-red (~605-625 nm) bands, for which the sensitivity of eye L

cones photoreceptors is enhanced with regards to that for red light emitted by Er^{3+} or Ho^{3+} at ~650-670 nm.[22] The upconversion processes of Yb^{3+}, Pr^{3+}-doped oxides have been studied only in a few number of single crystals,[23,24] polycrystalline material,[25] and micro/nanocrystals.[26,27]

Depending on the host different upconversion schemes can be expected for a same Ln^{3+}. The main factor of this dependence is the cut-off phonon energy value of the host, which can deeply affect the non-radiative de-excitation rates of NIR-excited Ln^{3+} states, thus the emission efficiency. The practical need of high luminescence efficiency for Ln-UCPs can be satisfied in matrices with low phonon energies, which minimize multiphonon de-excitation probabilities and thus non-radiative relaxations. Halide-based hosts have typically cut-off phonon energies lower than oxides, namely β-$NaYF_4$, ~400 cm^{-1};[28] KY_3F_{10}, ~500 cm^{-1};[29] YF_3, ~515 cm^{-1};[30] KPb_2Cl_5, ~203 cm^{-1};[31] but they show poorer chemical and photophysical stabilities than oxides, and additionally most of the synthesis routes described for nanocrystalline Ln^{3+}-doped halide-based UCPs are complex and often environmentally harmful. Oxyfluoride-based hosts constitute an intermediate option, with moderate cut-off phonon energies while maintaining good chemical stability. Among them, the yttrium oxyfluoride $Y_6O_5F_8$, an orthorhombic *Pbcm* Vernier phase within the general $Y_nO_{n-1}F_{n+2}$ series, presents some interesting structural characteristics, namely the four different crystal point sites for Y^{3+}, two with C_1 symmetry, one C_2 and one C_s.[32] Moreover, its ~650 cm^{-1} cut-off phonon energy,[33] allows expecting satisfactory upconversion efficiency. Further crystallographic information, a list with main Y-O, Y-F and Y-Y interatomic distances, is shown in Table S1 in the Supporting Information.

Although upconverted white light has been recently achieved in the $Y_6O_5F_8$ host, it has been done only by doping with the classical Yb^{3+}, Tm^{3+}, Er^{3+} combination.[17] Thus, one of the aims of this work is to demonstrate the interest of Yb^{3+}-sensitized, Pr^{3+}, Er^{3+} codoped $Y_6O_5F_8$ (hereafter Ln, Yb:$Y_6O_5F_8$) UCPs for selective light color emission and white light generation under DL NIR excitation. Moreover, the suitability of Er, Yb:$Y_6O_5F_8$ UCPs for high sensitivity ratiometric thermal sensing will be also shown. We have compared obtained results of the sensing sensitivity of Er^{3+} in $Y_6O_5F_8$ with corresponding data of the most efficient host, i.e., hexagonal β-$NaYF_4$ fluoride.[34,35] Ln, Yb:$Y_6O_5F_8$ samples have been currently prepared following a highly effective but simple procedure, namely by soft hydrothermal pH-controlled syntheses carried out in absence of any surfactant agent.

2 Experimental section

2.1 Preparation of samples

Yb^{3+}-sensitized oxyfluorides (2 mmol), i) doped with Er^{3+}, with composition $Y_{5.82}Yb_{0.12}Er_{0.06}O_5F_8$ (2 mol% Yb^{3+}, 1 mol% Er^{3+}), ii) codoped with Er^{3+} and Pr^{3+}, $Y_{5.874-t}Yb_{0.120}Er_{0.003}Pr_tO_5F_8$, (2 mol% Yb^{3+}, 0.05 mol% Er^{3+}, t = 0.012, 0.03, 0.045, 0.06, 0.09, 0.105 and 0.12, i.e., 0.2, 0.5, 0.75, 1.0 1.5, 1.75 and 2.0 mol% Pr^{3+}, respectively), and iii) doped with Pr^{3+}, $Y_{4.08}Yb_{0.12}Pr_{1.8}O_5F_8$ (2 mol% Yb^{3+}, 30 mol% Pr^{3+}), have been prepared by soft hydrothermal synthesis. Rare earth sesquioxides (Y_2O_3, Yb_2O_3, Er_2O_3 Strem Chemicals 99.9 %, Pr_2O_3 Cerac 99.9 %), and ammonium fluoride NH_4F (Merck 95 %) were used as starting reagents. Ln^{3+}-nitrates were firstly prepared by dissolving together the required stoichiometric amounts of corresponding sesquioxides in a solution of nitric acid (10 ml of distilled water and 10 ml of 69 % HNO_3), which was kept under heating until complete dryness. Then the Ln^{3+}-nitrates were dissolved in 10 ml of distilled water and added to a transparent solution of NH_4F in 20 ml of distilled water, the pH was adjusted to 9 with NH_4OH, and after 10 min of magnetic stirring the white suspension was transferred to a Teflon-lined autoclave, which was sealed and heated to 185 ºC during 24 h. The reaction was carried out without using external structure directing agents or organic templates, whose incomplete removal could compromise the optical emission efficiency. The product resultant from the hydrothermal reaction was collected by centrifugation, washed with ethanol several times, and overnight dried to 150 ºC in a desiccator, in each case. A subsequent 3 h annealing to 600 ºC was necessary to achieve the orthorhombic $Y_6O_5F_8$ phase (JCPDS File #80-1125).[36] Furthermore, the annealing removes defects typically associated to wet low-temperature synthesis methods, as oxygen vacancies and local lattice defects, and promotes a better crystallization.

For comparative purposes a sample of composition β-$NaY_{0.97}Yb_{0.02}Er_{0.01}F_4$ (i.e., with 2 mol% Yb^{3+} and 1 mol% Er^{3+}) was also prepared through a hydrothermal reaction, see its description in the Supplementary Information.

2.2 Characterization of samples

The characterization of the crystalline phase for each prepared oxyfluoride composition was carried out at room temperature by powder X-ray diffraction (XRD) performed in a Bruker AXS D-8 Advance diffractometer, using Cu K_α radiation.

Field emission scanning electron microscopy (FE-SEM) images and quantitative composition analyses by energy dispersive X-ray (EDX) spectroscopy were performed with a FEI NOVA SEM230 equipment with an accelerating voltage of 10 kV. Transmission electron microscopy (TEM) images were recorded with a JEOL 2000FXII microscope, accelerating voltage of 200 kV, and high resolution TEM (HRTEM) images with a JEOL model JEM-3000F microscope, working with accelerating voltage of 300 kV.

Chemical characterization by X-ray photoelectron spectroscopy (XPS) was carried out in ultrahigh vacuum (10^{-10} mbar) with a SPECS GmbH system operated with a non monochromatic Al/Mg anode (200 W, 12 kV). The energy of the photoionized electrons is determined with a PHOIBOS 150 9MCD detector with a step of 25 eV. The collected results have been treated to remove satellites, to account for background and line fits with the CasaXPS software. These measurements were conducted on a pressed pellet.

Room temperature FT-IR optical absorption was collected in the range 4000-250 cm^{-1} using a Fourier transform Nicolet 20SXC spectrophotometer. Optical absorption measurements were recorded at 300 and 6 K with a Varian 5E spectrophotometer. For the latter measurements a He closed-cycle cryostat connected to a suitable temperature controller was used. In both cases the oxyfluorides were mixed with spectroscopy grade KBr, and the mixture pressed to form a semitransparent pellet.

For thermal sensing, upconversion spectra of Er, Yb:$Y_6O_5F_8$ and Er, Yb:β-$NaYF_4$ samples were measured at temperatures in the range 291 K - 550 K. Upconversion spectra of Pr, Er, Yb:$Y_6O_5F_8$ samples were measured at room temperature. In all cases the upconversion was nominally excited at 978 nm with a fiber-ended LIMO 25 W diode laser (DL) module, whose emission band, with 3.5 nm of FWHM, shifts in the range 972.5-978 nm with the increase of the diode current. A collimating optics was attached to the fiber, and this output was focused by a lens on the sample set at 45º. To avoid any thermal heating induced by the DL excitation, in optical thermometry experiments the excitation was carried out in pulsed regime, with a duty cycle of 10 % DL and the DL power output was limited to 7 W, 15.7 $W{\cdot}cm^{-2}$ of power density. It was observed that by lowering the excitation power upconversion band shapes remained unchanged, which indicated the absence of thermal effects induced by the excitation power. For the study of the emission features of Pr, Er, Yb:$Y_6O_5F_8$ samples the DL was operated either continuous wave (cw) or pulsed with a selected duty cycle in the range 1-10%. The upconversion was collected at 45º (experimental set-up for optical thermometry), or at 90º (spectra of Pr, Er, Yb:$Y_6O_5F_8$ samples) of the excitation beam by a condenser lens, and further focused by a microscope

objective to the input optical fiber of a Spectral Products model SM440 spectrometer. The excitation laser light was removed from the detection system by a Edmund Optics PO:7MOD-11081 short-wavelength pass filter, with a transmission band between 402 and 838 nm. All emission results were corrected by the spectral response of our detection system. For the control of the sample temperature an Instec system, including a HCP302 hot&cold plate and a high precision mK1000 temperature controller, was used. The temperature stability was ±0.1 K, ±0.5 K and ± 1 K at 350 K, 373 K and 473 K, respectively. The actual temperature of the sample was independently measured with a Cr-Al thermocouple buried below the irradiated point. CIE 1931[37] color coordinates of Pr, Er, Yb:$Y_6O_5F_8$ samples were calculated from the spectrally corrected upconversion spectra using the standard color-matching functions, and by a Konica-Minolta CS200 radiometer. Results from both methods are similar.

3 Results and Discussion

3.1 Crystal phase, composition and sample morphology

Products obtained after the hydrothermal reaction result to be isostructural to the yttrium hydroxyfluoride $Y(OH)_{1.69}F_{1.31}$ phase, JCPDS File #80-2006,[36] see Figure 1a showing the powder XRD pattern of a selected sample. After thermal treatment at 600 ºC during 3 h, the observed Bragg peaks fully reproduce the sequence of *hkl* reflections of the Vernier phase $Y_6O_5F_8$, JCPDS File #80-1125,[36] and in no case additional lines have been detected, supporting the purity of the crystal phase and expected compositions from prepared nominal stoichiometries, see Figure 1b with XRD patterns of all prepared samples.

Figure 2 displays representative SEM, TEM and HRTEM images of Ln, Yb:$Y_6O_5F_8$ samples. They are constituted by highly crystalline micron-sized bundles, which are formed by porous tubular-like nanostructures, see Figure 2c. This porosity can be due to the removal of internal bubbles of H_2O and or hydroxyl groups by the thermal treatment after the hydrothermal synthesis. The clearly observed lattice fringe distances in the Figure 2d, 0.317 nm, which matches the (161) interplanar *d* spacing of $Y_6O_5F_8$, and the Fast Fourier Transform (FFT) image included as an inset in the latter Figure, evidence the crystallinity of prepared hydrothermal oxyfluorides.

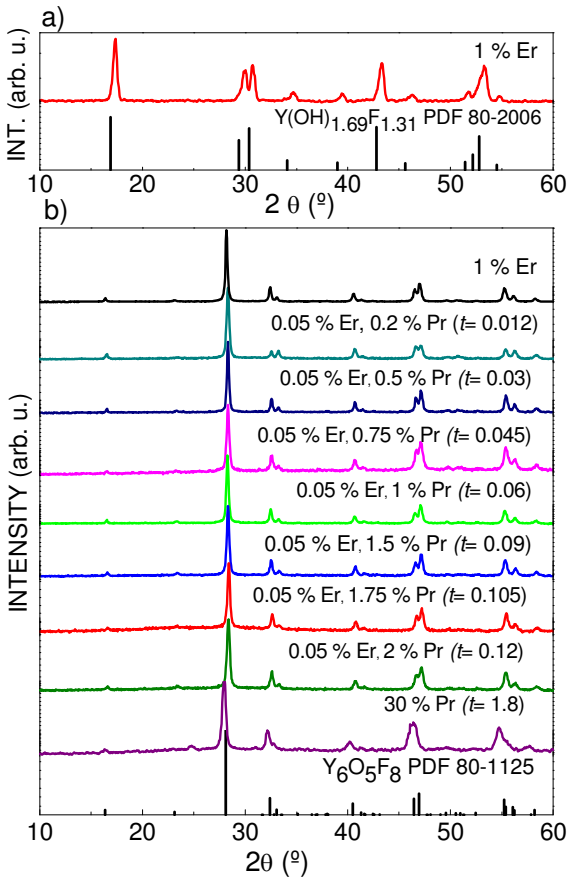

Figure 1. X-ray powder diffraction scans of: a) Er, Yb:$Y(OH)_{1.69}F_{1.31}$ obtained after the hydrothermal reaction, and for comparison the pattern scheme of hexagonal $Y(OH)_{1.69}F_{1.31}$ JCPDS File 80-2006; b) Yb^{3+}-sensitized (2 mol%), Ln^{3+}-doped $Y_6O_5F_8$ samples achieved after thermal treatment of previously obtained hydroxyfluorides, and for comparison the pattern scheme of orthorhombic *Pbcm*$Y_6O_5F_8$ JCPDS File 80-1125.

XPS and EDX analyses were carried out to verify valence state and homogeneous distribution of constitutive elements in formed microstructures of oxyfluoride samples. These results have been included in the Supplementary Information, Figure S1 and Table S2, for XPS data, and Figure S2, for EDX data.

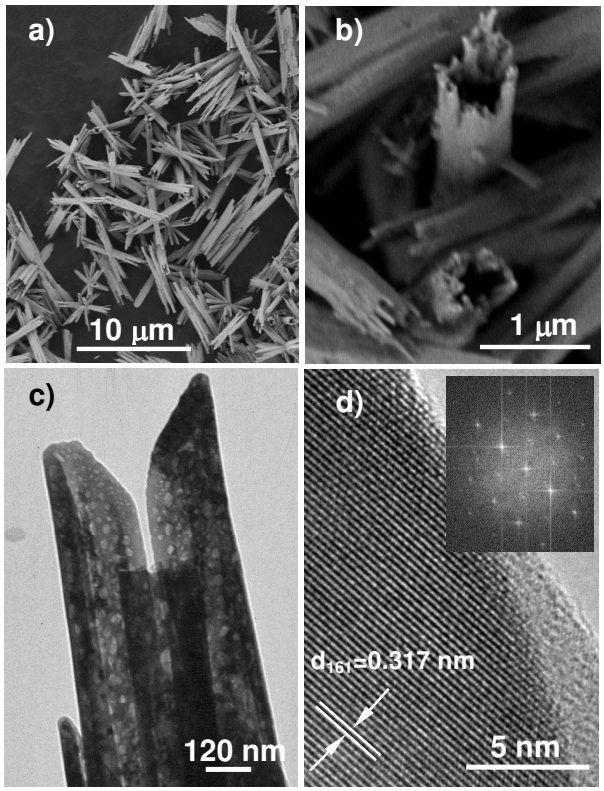

Figure 2. Images of Ln, Yb: $Y_6O_5F_8$: a) and b) SEM images of micron-sized bundles. c) TEM image of nanotubes forming the bundles. d) HRTEM image of a nanotube, and corresponding Fast Fourier Transform (FFT) image in the inset.

FT-IR spectra of representative Ln, Yb:$Y_6O_5F_8$ samples can be seen in Figure 3. The far infrared region 250-750 cm^{-1}, shown on the right side of the axis break, consists of a series of overlapped broad bands very similar to those previously observed for the undoped $Lu_{10}O_9F_{12}$ Vernier phase,[33] that can be assigned to vibronic modes of the $Y_6O_5F_8$ lattice. Small bands centered at 1630 cm^{-1} and 3440 cm^{-1} correspond to bending and stretching vibrations, respectively, of residual water, while very weak peaks only seen in the enlarged (x20) part of spectra at 880 cm^{-1}, ~1050 cm^{-1}, 1457 cm^{-1}, 2860 cm^{-1} and 2920 cm^{-1} are assigned to vibronic modes of ethanol,[38] that was used for washing the hydrothermal oxyfluorides.

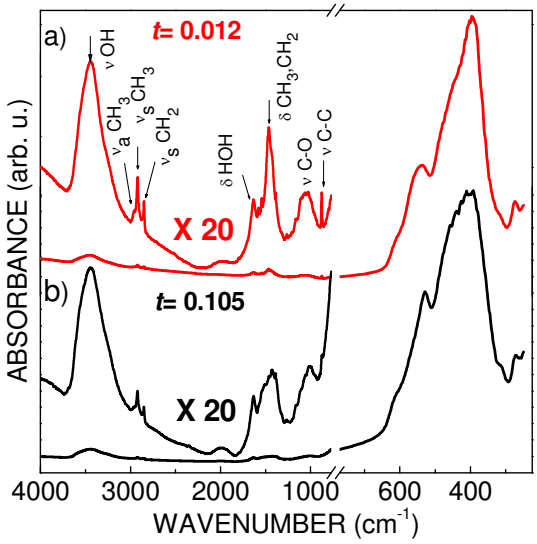

Figure 3. FT-IR spectra of hydrothermal $Y_{5.877-t}Yb_{0.12}Er_{0.003}Pr_tO_5F_8$ samples: a) t= 0.012, b) t= 0.105. For both prepared oxyfluorides enlarged views (x20) of the 4000-770 nm region at the left of axes break have been included.

For the formation of above described high aspect ratio tubular forms we propose a rolling-up mechanism favored by current hydrothermal conditions, acting over the highly anisotropic and layered structure of $Y_6O_5F_8$, see some views of the structure in the Figure 4. It is the well established mechanism for the formation of low-dimensional tubular products from the hydrothermal treatment of laminar composites, either these intercalated with long-chained organic molecules yielding V_2O_5-related nanotubes,[39] or these obtained directly from precursors, for instance, cubic sesquioxides Ln_2O_3,[40,41] and tetragonal $GdVO_4$.[42] The coexistence of scrolls rolled at different degrees, as can be seen in Figure 2c and Figure S3 supports this mechanism.

Concerning the characterization of the hydrothermal Er, Yb: β-$NaYF_4$ sample, Figure S4 shows its XRD pattern, in which only the Bragg peaks corresponding to the hexagonal $P6_3/m$ β-$NaYF_4$ phase are seen, and Figure S5 displays some SEM and TEM images.

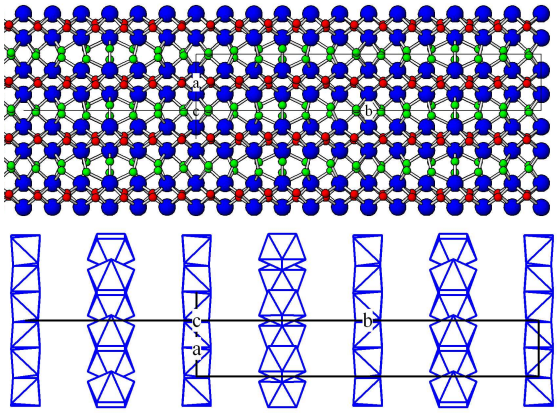

Figure 4. Views of the *ab* plane of the orthorhombic structure of the Vernier $Y_6O_5F_8$ phase (crystal data taken from the Collection Code 68950 of PHP-MySQL Inorganic Crystal Structure Database, Fachinformationszentrum, Karlsruhe. Blue, red and green balls represent Y, O and F atoms, respectively.

3.2 Ratiometric temperature sensing with Er, Yb:$Y_6O_5F_8$

3.2.1 Thermal evolution of upconversion spectra

An initial assessment of the role of both Yb^{3+} and Er^{3+} concentrations on the intensity of the visible NIR excited (~980 nm) upconversion of $Y_{6-x-y}Yb_xEr_yO_5F_8$ samples was carried out by varying firstly x in the range 0.12-0.9 (i.e. Yb^{3+} concentrations from 2 to 15 mol%) with y = 0.06 (i. e. Er^{3+} concentration 1 mol%), and then for the resulting best x by varying y from 0.012 to 0.12 (i.e. Er^{3+} concentration from 0.2 to 2 % mol). Optimised results were found to correspond to $Y_{5.82}Yb_{0.12}Er_{0.06}O_5F_8$ (2 mol% Yb^{3+}, 1 mol% Er^{3+}, hereafter Er, Yb:$Y_6O_5F_8$).

Visible upconversion spectra of the Er, Yb:$Y_6O_5F_8$ sample at measured temperatures in the 292 K - 532 K range consist of: i) Green emissions having two groups of well resolved maxima, the first one with peaks at 522 nm, 527 nm and 534 nm is assigned to $^2H_{11/2}\rightarrow{}^4I_{15/2}$ Er^{3+} transitions, and the second one with peaks at 547 nm and 554 nm that corresponds to $^4S_{3/2}\rightarrow{}^4I_{15/2}$ Er^{3+} transitions; ii) A strong red emission at 645-675 nm, originated from the $^4F_{9/2}\rightarrow{}^4I_{15/2}$ Er^{3+} transition. For convenience, Figure 5 includes a schematic representation of the distribution of the energy levels of Yb^{3+} and Er^{3+}, and electronic transitions giving rise to green and red Er^{3+} upconversion. Measured

upconversion spectra for the lowest (292 K) and highest (532 K) measured temperatures are shown in Figure 7a, from which the change in the relative intensity of these transitions with the temperature can be clearly appreciated, and Figure 6b presents a view of the evolution of green bands in the range of temperatures of physiological interest, 292 K - 323 K.

3.2.2 Assessment of thermal sensitivity: Discussion

Green upconversion mainly occurs through two successive near-resonant energy transfers (ET) from Yb^{3+} in $^2F_{5/2}$ state to Er^{3+}, the first exciting Er^{3+} to the intermediate $^4I_{11/2}$ state and then to $^4F_{7/2}$, although upconversion processes through Er^{3+} ions, ground state absorption (GSA) and excited state absorption (ESA), can also play a role. Green emitting levels $^2H_{11/2}$ and $^4S_{3/2}$ are populated by multiphonon relaxation from $^4F_{7/2}$. Furthermore, the red emitting $^4F_{9/2}$ state is also populated by non-radiative multiphonon relaxation from $^4F_{7/2}$, but the strong intensity of the red band points to further mechanisms also feeding $^4F_{7/2}$,[43,44] see their schemes at the left side in Figure 5.

Er^{3+} upconversion spectra in Figure 6a indicate a simultaneous development of the green emission from $^2H_{11/2}$ and the decrease of the emission from $^4S_{3/2}$ as the temperature rise from room temperature. This situation is understood as derived from the redistribution of the relative electronic population of $^4S_{3/2}$ and $^2H_{11/2}$ multiplets, which having relatively close energies are in thermal equilibrium governed by the Boltzmann law, $n_i = N \cdot \exp(-E_i/k_BT)$, being n_i the population of the level i, E_i its energy, N the total number of electrons of the system, k_B the Boltzmann constant, 8.6173×10^{-5} $eV \cdot K^{-1}$, and T the absolute temperature in Kelvin. Since the luminescence intensity of a given level is proportional to its electronic population, the intensity ratio R of the two thermally coupled Er^{3+} energy levels can be written as:

$$R = \frac{I_{^2H_{11/2}}}{I_{^4S_{3/2}}} \approx \frac{n_{^2H_{11/2}}}{n_{^4S_{3/2}}} = C \cdot \exp(-\Delta E / k_B T) \qquad (1)$$

where ΔE is the energy gap between $^4S_{3/2}$ and $^2H_{11/2}$, and the proportion has been converted to the equality by introducing the preexponential C constant, that includes dependencies on the degeneracy, spontaneous emission rates and energies of the emitting states in the host.[8,11]

Figure 7 shows the thermal dependence of the $^2H_{11/2}$ and $^4S_{3/2}$ intensity ratio R, calculated from integrated areas of corresponding bands (full triangles), along the whole measured temperature range. The exponential dependence on temperature indicated in Eq.

(1) was assessed by fitting LnR vs 1/T (open triangles), which gave values for C and ΔE of 7.4±0.1 and 598±4 cm^{-1}, respectively. Alternatively, by using heights of well resolved peaks at 522 nm ($^2H_{11/2}$) and 554 nm ($^4S_{3/2}$) to calculate R (Figure 7, squares) values of C=14.8±0.3 and ΔE=708±4 cm^{-1} have been obtained.

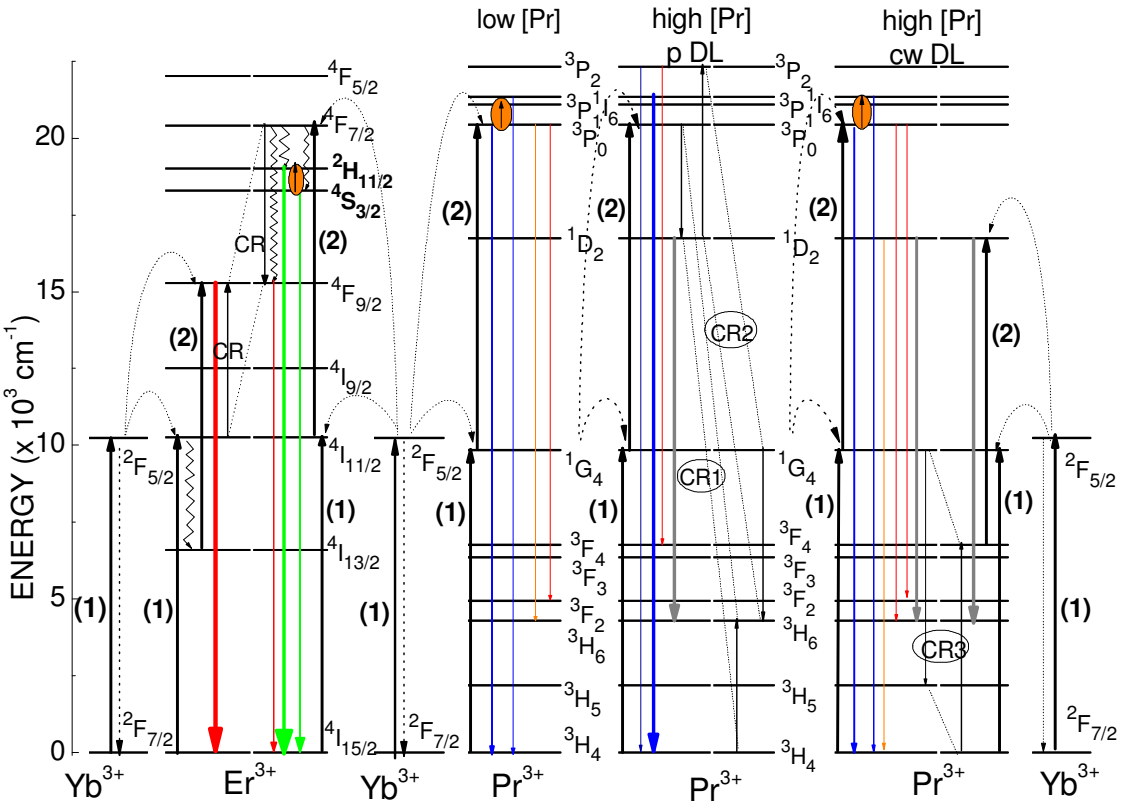

Figure 5. Schemes of Ln^{3+} = Yb^{3+}, Er^{3+} and Pr^{3+} electronic configurations in the $Y_6O_5F_8$ host. Pathways for ~978 nm excited upconversion in Yb^{3+}-sensitized (2 mol%) $Y_{5.82}Yb_{0.12}Er_{0.06}O_5F_8$ (1 mol% Er^{3+}), $Y_{5.847}Yb_{0.12}$ $Er_{0.003}Pr_{0.03}O_5F_8$ (0.05 mol% Er^{3+}, 0.5 mol% Pr^{3+}, low [Pr]) and $Y_{5.757}Yb_{0.12}Er_{0.003}Pr_{0.12}O_5F_8$ (0.05 mol% Er^{3+}, 2 mol% Pr^{3+}, high [Pr]) samples include (upward arrows) ground state absorptions (1), excited state absorption (2), and (dashed arrows) Yb^{3+}-Ln^{3+} resonant energy transfers. Upconversion emissions and their intensity distribution are illustrated by corresponding sets of downwards arrows. Schemes of cross-relaxations for populating emitting multiplets $^4F_{9/2}$ Er^{3+} (CR) and $^1D_2$ Pr^{3+} (CR1), $^3P_2$ Pr^{3+} (CR2), and $^3F_4$ Pr^{3+} (CR3) are also depicted.

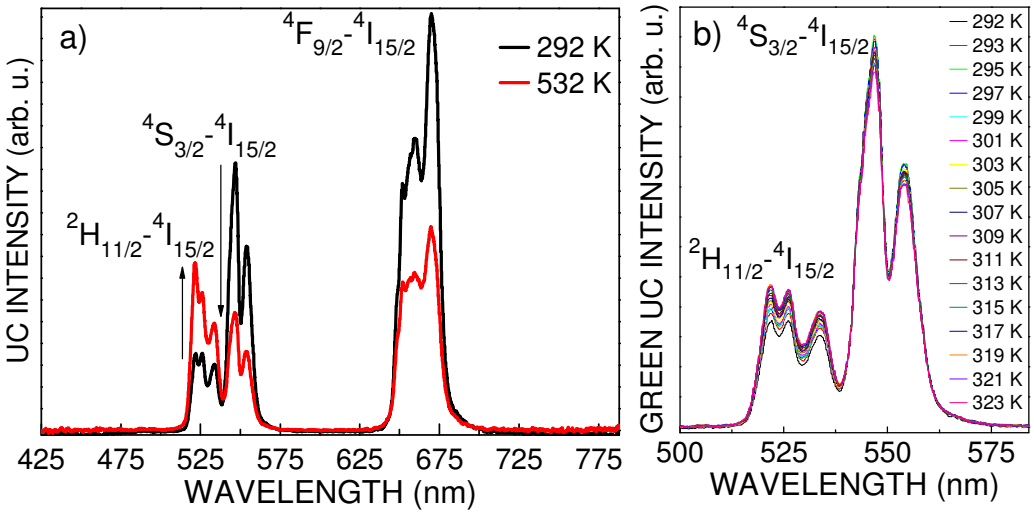

Figure 6. NIR excited (λ_{EXC} ~978 nm) upconversion spectra of $Y_{5.82}Yb_{0.12}Er_{0.06}O_5F_8$ (2 mol% Yb^{3+}, 1 mol% Er^{3+}) oxyfluoride: a) Comparison of the visible range of spectra at 292 K and 532 K, b) Evolution of green bands of $^2H_{11/2}$, $^4S_{3/2}\rightarrow{}^4I_{15/2}$ electronic transitions in the temperature range 292 K - 323 K.

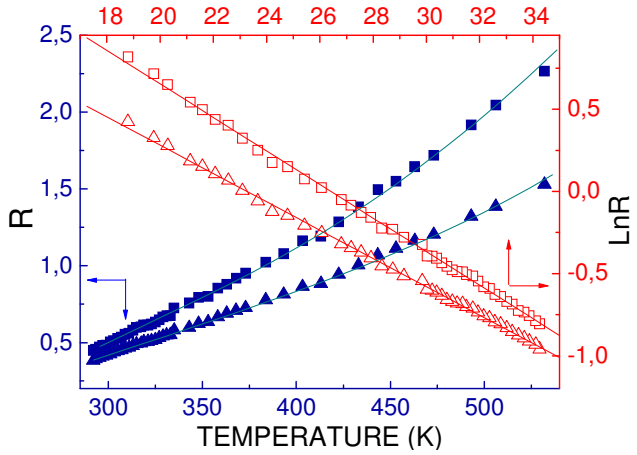

Figure 7. Exponential dependence of $R=I^2H_{11/2}/I^4S_{3/2}$ with the temperature in the 292 K- 532 K range, (full symbols), for Er, Yb:$Y_6O_5F_8$. R values were measured as integrated areas of green Er^{3+} bands (triangles) or as height of peaks at 522 nm ($^2H_{11/2}$) and 554 nm ($^4S_{3/2}$) (squares). From LnR vs 1/T plots (open symbols), best fits of above relationships were achieved (continuous lines).

For temperature sensing applications it is important to know the rate at which the measured temperature-sensitive parameter varies for a certain change in temperature. This rate is known as the sensitivity S of the thermal sensor, and when the measured parameter is R it is defined as:

$$S = \frac{\partial R}{\partial T} = C \cdot \left(\frac{\Delta E}{k_B T^2}\right) \exp(-\Delta E / k_B T) = R \cdot \left(\frac{\Delta E}{k_B T^2}\right) \qquad (2)$$

By using ΔE previously results derived from Figure 7 it is possible to calculate the thermal sensitivity S of Er, Yb:$Y_6O_5F_8$, which is presented in Figure 8, triangles for R calculated from integrated areas of $^2H_{11/2}$ and $^4S_{3/2}$ bands, or squares for R calculated from heights of peaks at 522 nm ($^2H_{11/2}$) and 554 nm ($^4S_{3/2}$). While for the first dataset S varies from $38.7 \cdot 10^{-4}$ K^{-1} to $46.7 \cdot 10^{-4}$ K^{-1}, for the second one S is clearly higher, from $53.5 \cdot 10^{-4}$ K^{-1} to $81.5 \cdot 10^{-4}$ K^{-1}.

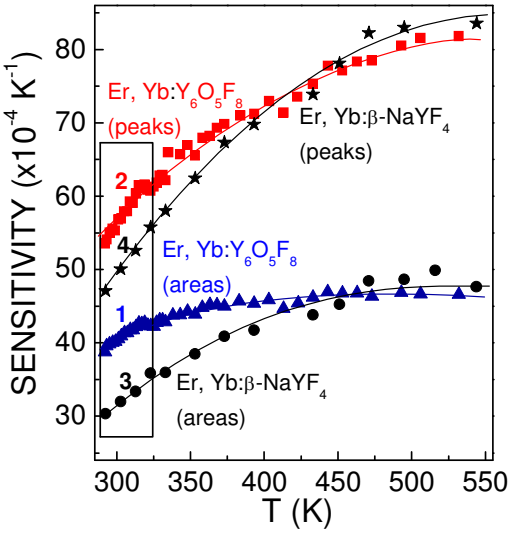

Figure 8. Sensitivity of Er, Yb:$Y_6O_5F_8$ thermal sensor: ratiometric evaluation of the intensity of upconverted green Er^{3+} emissions: 1, through integrated areas of bands (full triangles); 2, through heights of peaks at 522 nm ($^2H_{11/2}$) and 554 nm ($^4S_{3/2}$) (full squares). For comparison, the measured thermal sensitivity of Er, Yb:β-$NaYF_4$ has been included (3, from integrated areas of green bands, full circles; 4, from heights of peaks at 521.2 nm nm ($^2H_{11/2}$) and 546 nm ($^4S_{3/2}$), full stars). The underlined area corresponds to the physiological temperature range, 290 K- 323 K.

For Er,Yb:β-$NaYF_4$, the most efficient green upconverting material,[34] the thermal sensitivity derived from the $^2H_{11/2}$ to $^4S_{3/2}$ emission intensity ratio R can be found in the literature,[35] as well as for its polymorph Er,Yb:α-$NaYF_4$.[7] However, to establish more properly the comparison with the sensitivity of currently studied Er, Yb:$Y_6O_5F_8$, upconversion spectra of also prepared Er, Yb:β-$NaYF_4$ have been measured with the same experimental set up, in the same temperature range. In Supporting Information Figure S6a shows the evolution of NIR excited upconversion green bands corresponding to $^2H_{11/2}$, $^4S_{3/2} \rightarrow {}^4I_{15/2}$ electronic transitions of hydrothermal Er, Yb:β-$NaYF_4$ in the temperature range

292 K - 544 K, and a simplified view with spectra of lowest and highest measured temperatures is displayed in Figure S6b. Figure S6c gives the thermal dependence of R, with R values calculated using either integrated areas of green bands or heights of individual well-resolved peaks for $^2H_{11/2}$ and $^4S_{3/2}$, as well as corresponding expressions for best fits of LnR vs 1/T in each case.

The comparison of the currently measured thermal sensitivity of Er,Yb:β-$NaYF_4$ with that of Er,Yb:$Y_6O_5F_8$ appears in Figure 8. It can be seen that for similarly extracted R data, that is, either integrated areas (circles for Er,Yb:β-$NaYF_4$; triangles for Er,Yb:$Y_6O_5F_8$), or alternatively heights of individual peaks (stars for Er,Yb:β-$NaYF_4$; squares for Er,Yb:$Y_6O_5F_8$), the oxyfluoride phase always compares favorably with the fluoride for temperatures below 450 K, and especially in the temperature range of physiological interest 295 K - 323 K.

3.3 Selection of NIR excited upconverted light color in Pr, Er, Yb:$Y_6O_5F_8$ oxyfluorides

Besides the green bands, the room temperature upconversion spectrum of 1 mol% Er^{3+}, 2 mol% Yb^{3+}:$Y_6O_5F_8$ shows a strong, in fact dominating, red emission from the $^4F_{9/2}\rightarrow{}^4I_{15/2}$ Er^{3+} electronic transition, see previous Figure 6a. Its high intensity indicates upconversion mechanisms that populate $^4F_{9/2}$ in addition to non-radiative decay from the $^4S_{3/2}$ state,[43,44] i.e., the cross-relaxation (CR) process [$^4F_{7/2}$, $^4I_{11/2}$]→[$^4F_{9/2}$, $^4F_{9/2}$] that bypasses $^2H_{11/2}$ and $^4S_{3/2}$ levels, and whose efficiency is enhanced by the current high Er^{3+} concentration, as well as a second ET from Yb^{3+} ($^2F_{5/2}$) to Er^{3+} ($^4I_{13/2}$), after efficient non-radiative decay from $^4I_{11/2}$, see schemes depicted in the left part of Figure 5.

Thus, the generation of white light by RGB intensity balance in the $Y_6O_5F_8$ host can be reasonably achieved by incorporating a blue emitting Ln^{3+} cation to the Er^{3+}-Yb^{3+} combination. We have now analyzed the possibilities offered by Pr^{3+}-Er^{3+} codoping, as an alternative to the earlier studied Tm^{3+}-Er^{3+} combination.[17]

The specific characteristic of the currently studied oxyfluoride structure, namely the Y^{3+}(Ln^{3+}) multisite character (see Table S1 and results concerning Pr^{3+} sites in $Y_6O_5F_8$ from absorption spectra at 6 K, Figure S7), with a cloud of short Y-Y distances, as short as 3.5730 Å,[32] is the origin of the observed inhomogeneous broadening of optical spectra for current oxyfluorides. In fact, even in the low temperature optical absorption spectrum of Pr, Yb: $Y_6O_5F_8$, Figure S7, the bands are broader than those usually observed for Pr^{3+}-doped crystalline hosts, like structurally ordered oxides[45,46] fluorides,[47] and also in disordered

oxides.[48] Furthermore, this structural characteristic suggests a crucial role for the Ln^{3+} concentration in achieving the critical Ln-Ln distance that favors energy transfer and cross-relaxation (CR) processes, thus in the relative intensity of the observed upconversion transitions, which are moreover strongly sensitive to the optical excitation power. To properly explore these relationships, upconversion spectra of samples with $Y_{5.877-t}Yb_{0.12}Er_{0.003}Pr_tO_5F_8$ composition, in which Yb^{3+} and Er^{3+} concentrations are 2 mol% and 0.05 mol%, respectively, and the Pr^{3+} concentration varies in the range $0.012 \leq t \leq 0.12$ (0.2 to 2.0 mol%) were measured under DL excitation power densities from 155 $W{\cdot}cm^{-2}$ to 1098 $W{\cdot}cm^{-2}$, in both pulsed and cw excitation regimes. Figures 9 and 10 show the comparison of upconversion spectra for $Y_{5.847}Yb_{0.12}Er_{0.003}Pr_{0.03}O_5F_8$ (0.5 mol% Pr^{3+}) and $Y_{5.757}Yb_{0.12}Er_{0.003}$ $Pr_{0.12}O_5F_8$ (2.0 mol% Pr^{3+}) samples, respectively, selected as representative compositions for low and high Pr-doped samples, in both cases under diverse pulsed and cw excitation conditions. Previous Figure 5 also includes schematic representations of the distribution of energy levels of Yb^{3+} and Pr^{3+}, and electronic transitions involved in observed upconversion emissions.

3.3.1 NIR excited upconversion in low Pr-doped, Er, Yb:$Y_6O_5F_8$ oxyfluorides

For low Pr^{3+} concentration, sample $Y_{5.847}Yb_{0.12}Er_{0.003}Pr_{0.03}O_5F_8$, the NIR-excited upconversion spectrum consists of emissions from both Pr^{3+} and Er^{3+} activators: i) A very weak blue contribution at 477 nm, that corresponds to $^3P_1(+^1I_6)\rightarrow{}^3H_4$ Pr^{3+} emissions, along with an intense blue band with peaks at 490 nm and 497 nm corresponding to $^3P_0\rightarrow{}^3H_4$ Pr^{3+} emission, the structure of this band being most likely due to transitions to different Stark levels of the $^3H_4$ multiplet, see Figure S7. ii) The green band corresponding to $^2H_{11/2}$,$^4S_{3/2}\rightarrow{}^4I_{15/2}$ Er^{3+} emissions, already described in the earlier Section; iii) An orange band peaking at 619 nm, $^3P_0\rightarrow{}^3H_6$ Pr^{3+}; iv) Red bands in the range 650-678 nm, with maxima at 655 nm and 670 nm, which correspond to $^3P_0\rightarrow{}^3F_2$ Pr^{3+} and $^4F_{9/2}\rightarrow{}^4I_{15/2}$ Er^{3+} overlapped transitions, see Figure 9. The comparison between pulsed and cw excited upconversion spectra in Figure 9 shows that although with similar distribution of energy, the relative intensities of these peaks strongly depend on the strength and type (pulsed or cw) of the DL excitation. In pulsed excited upconversion spectra dominating transitions are from $^3P_0$ Pr^{3+} and from $^4S_{3/2}$ Er^{3+} states, and bands from $^3P_1(+^1I_6)$ Pr^{3+} and from $^2H_{11/2}$ Er^{3+} are very weak and of medium intensity, respectively. Under high cw excitation power a progressive development of emissions from latter states is observed, being especially noteworthy for $^2H_{11/2}$ Er^{3+}.

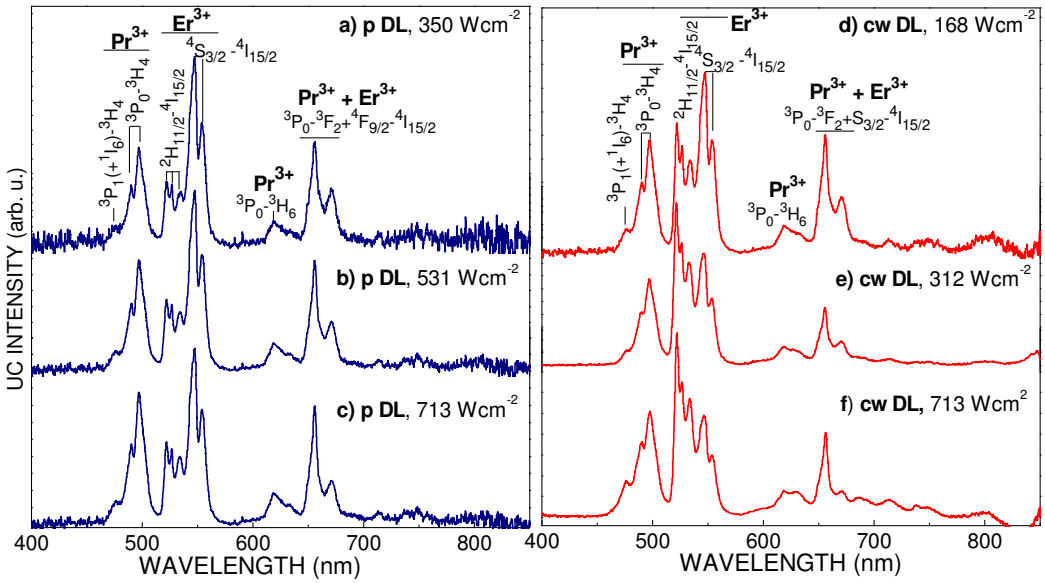

Figure 9. Upconversion spectra of $Y_{5.847}Yb_{0.12}Er_{0.003}Pr_{0.03}O_5F_8$ (0.5 mol% Pr^{3+}) under DL excitation at ~978 nm: Pulsed DL, with power density of a) 350 W·cm^{-2}, b) 531 W·cm^{-2}, and c) 713 W·cm^{-2}. Cw DL excitation with power density of d) 168 W·cm^{-2}, e) 312 W·cm^{-2} and f) 713 W·cm^{-2}.

3.3.2 NIR-excited upconversion in high Pr-doped, Er, Yb:$Y_6O_5F_8$ oxyfluorides

For high Pr^{3+} concentration, $Y_{5.757}Yb_{0.12}Er_{0.003}Pr_{0.12}O_5F_8$, the upconversion spectra show differences with those described above, see Figure 10. For low enough NIR excitation power density, 155 W·cm^{-2}, both in pulsed (Figure 10a) and cw (Figure 10d) regimes, the spectra show: i) Two blue bands, the first at 454 nm, $^3P_2 \rightarrow {}^3H_4$ Pr^{3+} transition, and a second more intense with main maxima at 474 nm and 477 nm, $^3P_1(+{}^1I_6) \rightarrow {}^3H_4$ Pr^{3+} transitions. ii) A very weak red peak at ~650 nm that corresponds to the $^3P_2 \rightarrow {}^3F_4$ Pr^{3+} transition. iii) A strong IR band centered at ~800 nm, the $^1D_2 \rightarrow {}^3H_6$ Pr^{3+} transition. The latter IR band was not observed previously in oxyfluoride samples, neither with Er^{3+} nor with low Pr^{3+} concentration, Figures 6 and 9, respectively. Also it is worth noticing the complete absence of Er^{3+} green emissions, in contrast to the intense bands observed in Figure 9. By increasing the pulsed excitation power density, together with the above described peaks, the blue band, $^3P_0 \rightarrow {}^3H_4$ Pr^{3+} transition, the green band, $^2H_{11/2}$, $^4S_{3/2} \rightarrow {}^2I_{15/2}$ Er^{3+} transitions, and several orange $^1D_2 \rightarrow {}^3H_4$ Pr^{3+}, $^3P_0 \rightarrow {}^3H_6$ Pr^{3+} and red bands, $^3P_0 \rightarrow {}^3F_2$ Pr^{3+}, begin to be observed, and their intensities experience a progressive development with the increase in power density strength.

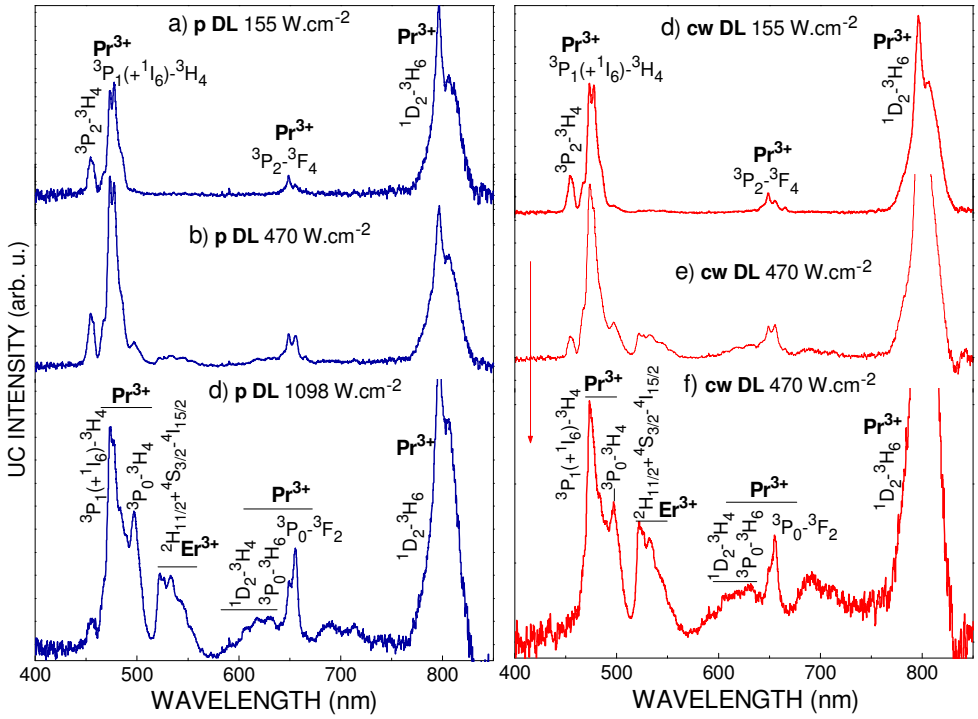

Figure 10. Upconversion spectra of $Y_{5.757}Yb_{0.12}Er_{0.003}$ $Pr_{0.12}O_5F_8$ (2.0 mol% Pr^{3+}) under DL excitation at ~978 nm: Pulsed DL, with power density of: a) 155 W·cm^{-2}, b) 470 W·cm^{-2}, and c) 1098 W·cm^{-2}. Cw DL with power density of: d) 155 W·cm^{-2}, e) 470 W·cm^{-2} and f) 470 W·cm-^{2}, steady-state.

By changing the NIR excitation to the cw regime on the same $Y_{5.757}Yb_{0.12}Er_{0.003}$ $Pr_{0.12}O_5F_8$ composition, the general evolution of upconversion spectra with the power density strength is similar but faster than that in pulsed excited spectra. A first spectrum collected under enough moderate power density, 470 W·cm^{-2}, shows relative intensities of blue, green and red bands still quite similar to those observed under the same power density pulsed excitation, compare Figures 10e and 10b, but in the cw excited 470 W·cm^{-2} steady-state UC spectrum these visible bands are like those in the 1098 W·cm^{-2} pulsed excited upconversion spectrum, compare Figures 10f and 10c. On the other hand, under cw excitation the IR $^1D_2 \rightarrow {}^3H_6$ Pr^{3+} emission is getting stronger than in the pulsed excitation regime, compare Figures 10e and 10f (cw excited spectra), and 9b and 9d (pulsed excited spectra).

3.3.3 Excitation and de-excitation pathways in Pr, Er, Yb:$Y_6O_5F_8$ oxyfluorides: Discussion

To better understand the origin of above pointed out differences in upconversion spectra of $Y_{5.877-t}Yb_{0.12}Er_{0.003}Pr_tO_5F_8$ samples, Figure 5 has included the Yb^{3+}-Pr^{3+} excitation and de-

excitation pathways separately for low and high Pr^{3+} concentration. Independently of the considered Pr^{3+} concentration, the intermediate $^1G_4$ Pr^{3+} state is efficiently populated by resonant energy transfer from an $^2F_{5/2}$ excited Yb^{3+} ($^2F_{5/2}$, $^3H_4$)→($^2F_{7/2}$, $^1G_4$). Later on, in low Pr-doped samples the absorption of a second NIR ~978 nm photon excites Pr^{3+} from $^1G_4$ to $^3P_0$ (excited-state absorption ESA). Observed bands at blue, orange and red wavelengths under pulsed DL excitation at low power density can be explained on the basis of emission transitions from $^3P_0$ Pr^{3+} to $^3H_4$, $^3H_6$ and $^3F_2$, respectively, see Figure 5. The increase of the excitation power density, especially under cw DL excitation, heats the sample and induces the redistribution of the relative electronic populations of thermally coupled levels of Pr^{3+} and Er^{3+}, that further populates $^3P_1$(+$^1I_6$) above $^3P_0$ and $^2H_{11/2}$ above $^4S_{3/2}$, respectively. It leads to the observed development of the short wavelength side of the blue and green bands, i.e., emissions from $^3P_1$(+$^1I_6$) and $^2H_{11/2}$, respectively, associated to a parallel decrease in the intensity of the long wavelength wing, i.e., emissions from $^3P_0$ and $^4S_{3/2}$, respectively, which results to be especially remarkable for the green band, see Figure 9f. Thus, strong cw DL excitation represents "hot" exciting conditions, while low power density pulsed DL excitation is able to keep the sample at temperatures near room temperature, and therefore represents "cold" exciting conditions

In contrast, in samples with high Pr^{3+} concentration excited with DL NIR low power density, 155 W·cm^{-2}, in both pulsed and cw regimes, emissions from Er^{3+} are completely quenched, and those from $^3P_0$ Pr^{3+} are absent. In this case the blue light is emitted from $^3P_2$ and $^3P_1$(+$^1I_6$) Pr^{3+} multiplets. This fact as well as the strong IR emission at ~800 nm, $^1D_2$→$^3H_6$ Pr^{3+}, point to a very effective $^3P_0$→$^1D_2$ Pr^{3+} non-radiative decay in this system. Several mechanisms have been proposed for this decay: multiphonon relaxation,[49] [$^3P_0$, $^3H_4$]→[$^1D_2$, $^3H_6$] cross-relaxation between pairs of interacting Pr^{3+} ions,[50,51,52] relaxation *via* intersystem crossing through a low-lying 4*f*5*d* excited state of Pr^{3+},[48,53] and intersystem tunneling through a low-lying Pr-to metal charge-transfer state (virtual charge exchange model).[54] $^3P_0$ to $^1D_2$ multiphonon relaxation rate is weak because more than six host phonons are required to fill the energy gap between these multiplets. Taking into account that cross-relaxation (CR) processes are favored by the high Pr^{3+} concentration, the quenching of the $^3P_0$ emission is likely due to the improvement of the [$^3P_0$, $^3H_4$]→[$^1D_2$, $^3H_6$] CR efficiency to populate $^1D_2$ with the increase of the Pr^{3+} concentration,[26,50,52] see this proposed CR1 scheme in Figure 5. On the other hand, the sequential two-photon absorption process for 978 nm photons does not supply enough energy to populate $^3P_2$. However, there

are several cross-relaxation processes that can be considered to fed $^3P_2$ from $^1D_2$, namely [$^1D_2$, $^1D_2$]→[$^3P_2$, $^1G_4$],[24] [$^1D_2$, $^3F_2$]→[$^3P_2$, $^3H_4$],[55] and the resonant [$^1D_2$, $^1G_4$]→[$^3P_2$, $^3H_6$], see the scheme for this latter process, CR2, in Figure 5. Then emitting $^3P_1$(+$^1I_6$) multiplets are populated by non-radiative relaxation decay from $^3P_2$.

In the pulsed regime, the increase of the DL NIR excitation power density fasten the non-radiative decay from $^3P_2$ to $^3P_1$(+$^1I_6$) and $^3P_0$, which would explain the development of blue and red emissions from $^3P_0$, see Figure 10b corresponding to the sample under 470 W·cm^{-2} pulsed excitation power density. Furthermore, the increase of the excitation power produces a significant development of the green emission $^2H_{11/2}$, $^4S_{3/2}$→ $^4I_{15/2}$ Er^{3+}, that arises mostly from the thermally populated higher energy $^2H_{11/2}$ state, as it is indicated by the observed thermal evolution of these states in Figure 6a.

The presence of well developed emissions from $^3P_0$ along with the increase of intensity of the NIR emission from $^1D_2$ observed in upconversion spectra of "hot" samples in both the steady-state under cw excitation of 470 W·cm^{-2}, Figure 10f, and under 1098 W·cm^{-2} power density in the pulsed regime, Figure 10c, point to an additional pathway for further population of the $^1D_2$ multiplet. Such pathway can start with the population of the intermediate $^3F_4$ through the CR3 cross-relaxation ($^1G_4$, $^3H_4$)→($^3H_5$, $^3F_4$), and then by the absorption of the second 978 nm photon in the $^3F_4$ multiplet (ESA),[47] see the corresponding scheme in Figure 5.

3.3.4 CIE color coordinates of Pr, Er, Yb:$Y_6O_5F_8$ oxyfluorides

Figure 11 illustrates the variation of the CIE color coordinates with the Pr^{3+} concentration along the prepared oxyfluoride $Y_{5.877-t}Yb_{0.120}Er_{0.003}Pr_tO_5F_8$ series, for two particular DL cw pumped power densities, namely 155 W·cm^{-2} and 470 W·cm^{-2}. The CIE coordinates correspond to steady-state upconversion spectra ("hot" samples). Alternatively, Figure 12a shows the evolution of CIE color coordinates for the two representative $Y_{5.847}Yb_{0.12}Er_{0.003}Pr_{0.03}O_5F_8$ (0.5 mol% Pr) and $Y_{5.757}Yb_{0.12}$ $Er_{0.003}Pr_{0.12}O_5F_8$ (2 mol% Pr) samples under cw pumped power densities in the range between 155 and 713 W·cm^{-2} (steady-state, "hot" samples), as well as CIE color coordinates for the higher Pr-doped sample under DL pulsed excitation ("cold" samples). Figures 12b and 12c show photographs taken with a digital camera without any filter of the bluish-green light emission from $Y_{5.847}Yb_{0.12}Er_{0.003}Pr_{0.03}O_5F_8$ (cw excitation of 784 W·cm^{-2} power density) and of the white light from $Y_{5.757}Yb_{0.12}$ $Er_{0.003}Pr_{0.12}O_5F_8$ (pulsed excitation of 627 W·cm^{-2} power density).

Beyond experimental uncertainties, the general rule is that almost independently of the excitation power, samples with low Pr^{3+} concentration ($t < 0.045$) emit green light, that is, the intensity of Er^{3+} green bands predominates even if Er^{3+} concentration is about one order of magnitude lower, while the light from samples with medium Pr^{3+}-doping level (typically those with $t = 0.045$, 0.75 mol% Pr, to $t = 0.105$, 1.75 mol% Pr) has bluish-green color, due to the intensity increase of blue emission of Pr^{3+}, and finally the sample with highest Pr^{3+} concentration ($t = 0.12$, 2.0 mol% Pr) can emit blue light under pulsed DL excitation ("cold" sample), with complete quenching of any Er^{3+} emission, or white light in the steady-state reached under cw DL excitation ("hot" sample), with CIE coordinates very close to the achromatic point (0.29, 0.30), (0.29, 0.35) and (0.31, 0.36), for 155, 312, and 470 $W \cdot cm^{-2}$, respectively, in this case by RGB mixing of emissions from both Pr^{3+} and Er^{3+}, being their concentration ratio of 40:1.

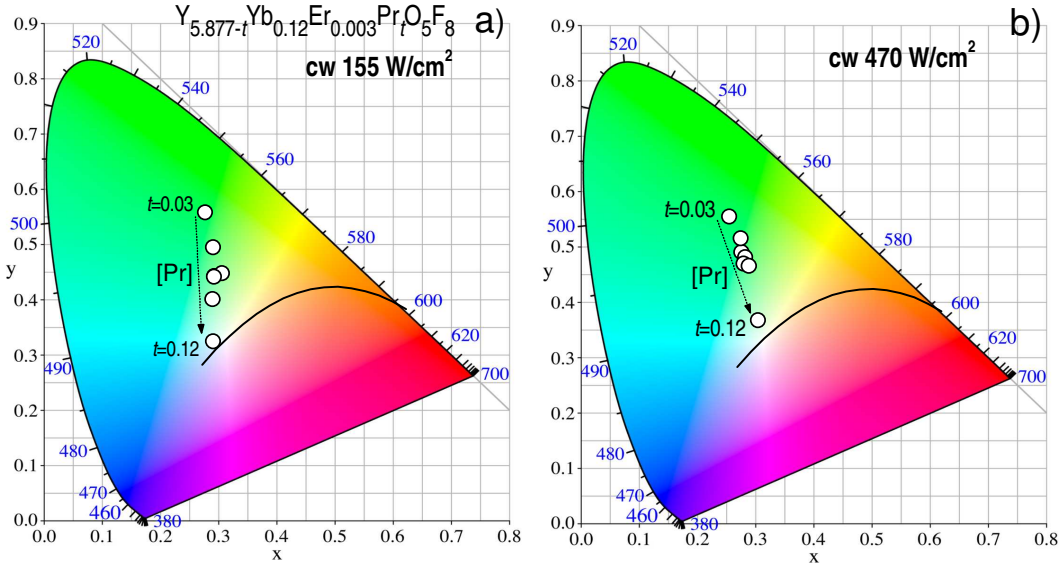

Figure 11. Variation of CIE color coordinates in the oxyfluoride series $Y_{5.877-t}Yb_{0.120}Er_{0.003}Pr_tO_5F_8$, $t = 0.03$ to 0.12, under DL NIR cw excitation at ~978 nm, with power density of: a) 155 $W \cdot cm^{-2}$, b) 470 $W \cdot cm^{-2}$. The arrows indicate increasing Pr^{3+} concentration [Pr]. The black line corresponds to the black-body radiation curve.

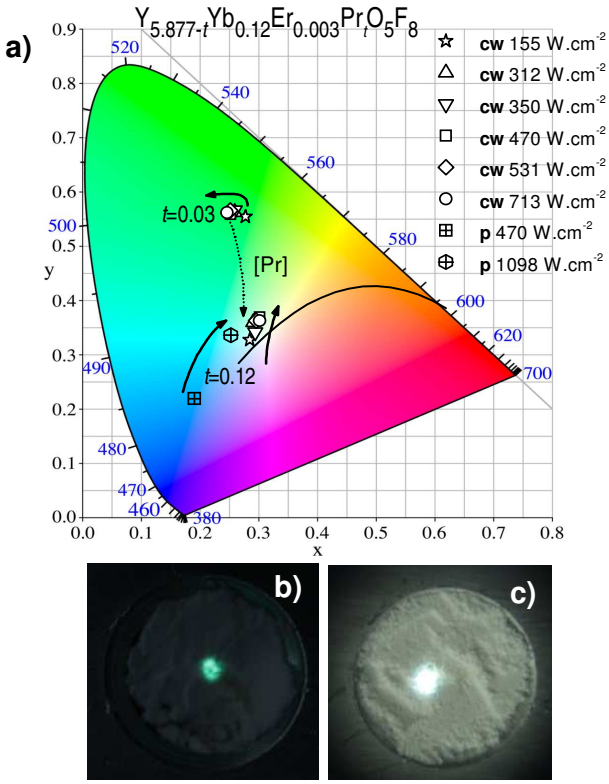

Figure 12. Variation of the CIE color coordinates in the oxyfluoride series $Y_{5.877-t}Yb_{0.120}Er_{0.003}Pr_tO_5F_8$, t = 0.03 to 0.12, under DL NIR cw excitation at ~978 nm, with power density of: a) 155 W·cm^{-2}, b) 470 W·cm^{-2}. The arrows indicate increasing Pr^{3+} concentration [Pr]. The black line corresponds to the black-body radiation curve.

4 Conclusions

Micron-sized bundles of highly crystalline individual nanotubes of Ln, Yb:$Y_6O_5F_8$ oxyfluorides have been prepared through an efficient low-temperature hydrothermal synthesis.

The ratiometric analysis of the thermal evolution of intensities of Er, Yb:Y_6O_5 NIR excited (~978 nm) green upconverted emissions from thermally coupled $^2H_{11/2}$ and $^4S_{3/2}$ Er^{3+} multiplets indicates thermal sensing potential with better sensitivity (S ~41·10^{-4} K^{-1}) than Er, Yb:β-$NaYF_4$ (S ~32·10^{-4} K^{-1}) in the temperature range of physiological interest. Additionally, we also demonstrated that the simplified analysis of the thermal evolution of green bands by using heights of individual well-resolved maxima for $^2H_{11/2}$ (at 522 nm) and $^4S_{3/2}$ (at 552 nm) allows substantial increase of sensitivity in thermal sensing with Er, Yb:$Y_6O_5F_8$.

Under NIR excitation the room temperature upconversion of isolated Ln^{3+} centers in low Ln-doped Yb:$Y_6O_5F_8$ samples is mainly related to $^3P_0$ Pr^{3+} and $^4S_{3/2}$ Er^{3+} radiative transitions, which produce blue, green, orange and red emissions, being predominant the green ones. The increase of the excitation power density, and the subsequent heating of the sample, promotes emissions from $^3P_1(+^1I_6)$ Pr^{3+} and $^2H_{11/2}$ Er^{3+} multiplets in thermal equilibrium with $^3P_0$ and $^4S_{3/2}$, respectively. By increasing the Pr^{3+} concentration, privileged upconversion transitions are the IR transition from $^1D_2$ Pr^{3+}, which is specific of high concentrated Pr^{3+} samples, and also the blue ones from $^3P_2$ and $^3P_1(+^1I_6)$ Pr^{3+} multiplets. For high Pr^{3+}-concentrated samples, the emission from $^3P_0$ Pr^{3+} and emissions from Er^{3+} are completely quenched at moderate excitation power density, but they can be recovered by increasing the excitation power, which induces further green, orange and red emissions. The strong sensitiveness of the upconversion behavior to the Pr^{3+} concentration, and for high Pr^{3+}-doped samples also to the NIR excitation power density, offer the opportunity for light color selection and white light generation by appropriate RGB intensity balance with Pr, Er, Yb:$Y_6O_5F_8$ oxyfluoride nanotubes.

Electronic Supporting Information Available: Table S1: Selected bond distances lengths for $Y_6O_5F_8$. Description of the hydrothermal preparation of Er (1 mol%), Yb (2 mol%):β-$NaYF_4$ sample. Results of XPS analysis of $Y_6O_5F_8$, with Figure S1: XPS spectra $Y_6O_5F_8$ and Table S2: Data from XPS analysis. Figure S2: EDX elements color maps and quantitative analysis of $Y_{4.08}Yb_{0.12}Pr_{1.8}O_5F_8$. Figure S3: Additional TEM images of Ln, Yb:$Y_6O_5F_8$ scrolls rolled at different degrees. Figure S4: XRD scan of hydrothermal Er, Yb:β-$NaYF_4$ sample. Figure S5: SEM and TEM images of hydrothermal Er, Yb:β-$NaYF_4$ sample. Figure S6: Upconversion spectra of Er, Yb:β-$NaYF_4$ for temperatures in the range 292 K to 544 K, and ratiometric intensity analyses of Er^{3+} green bands. Figure S7: Optical absorption spectra of Pr^{3+} in Pr (30 mol%), Yb:$Y_6O_5F_8$ at room temperature and at 6 K.

Acknowledgements

This work was supported by the Spanish Ministry of Economy and Competitiveness under project MAT2011-29255-C02-01.

References

1 W. Kim, M. Nyk, P. Prasad, *Nanotechnology* 2009, **20**, 185301.

2 M. Wang, C. C. Mi, W. X. Wang, C. H. Liu, Y. F. Wu, Z. R. Xu, C. B. Mao, S. K. Xu, *ACS Nano*, 2009, **3**, 1580-1586.

3 Y. Liu, D. Tu, H. Zhu, X. Chen, *Chem. Soc. Rev.* 2013, **42**, 6924-6958.

4 F. Wang, X. Liu, *Chem. Soc. Rev.* 2009, **38**, 976-98.

5 D. Jaque, F. Vetrone, *Nanoscale*, 2012, **4**, 4301-4326.

6 C.D.S. Brites, P.P. Lima, N.J.O. Silva, A. Millán, V.S. Amaral, F. Palacio, L.D. Carlos, *Nanoscale* 2012, **4**, 4799.

7 F. Vetrone, R. Naccache, A. Zamarron, A. Juarranz de la Fuente, F. Sanz-Rodríguez, L. Martínez Maestro, E. Martín Rodriguez, D. Jaque, J. García Solé, J. A. Capobianco, *ACS Nano* 2010, **4**, 3254-3258.

8 S.A. Wade, S.F. Collins, G.W. Baxter, *J. Appl. Phys.* 2003, **94**, 4743-4756.

9 L. H. Fischer, G. S. Harms, O. S. Wolfbeis, *Angew. Chem. Int. ed.* 2011, **50**, 45-4551.

10 H. Kusama, O. J. Sovers, T. Yoshioka, *Jpn. J. Appl. Phys.* 1976, **15**, 2349-2358.

11 H. Berthou, C.K. Jörgensen, *Opt. Lett.* 1990, **15**, 1100-1102.

12 L. Li, C. Guo, S. Jiang, D.K. Agrawal, T. Li, *RSC Adv.* 2014, **4**, 6391-6396.

13 X. Han, J. Maiz, C. Mijangos and C. Zaldo, *Nanotechnology* 2014, **25**, 205302.

14 M. Haase, H. Schäfer, *Angew. Chem. Int. Ed.* 2011, **50**, 5808-5829.

15 K. Zheng, D. Zhang, D. Zhao, N. Liu, F. Shi, W. Qin, *Phys. Chem. Chem. Phys.* 2010, **12**, 7620-7625.

16 Y. Zhang, J. Hao, *J. Appl. Phys.* 2013, **113**, 184112.

17 S. Wang, R. Deng, H. Guo, S. Song, F. Cao, X. Li, S. Su, H. Zhang, *Dalton Trans.* 2010, **39**, 9153-9158.

18 V. Mahaligan, R. Naccache, F. Vetrone, J. A. Capobianco, *Opt. Express* 2012, **20**, 111-119.

19 E. W. Barrera, M. C. Pujol, J. J. Carvajal, X. Mateos, R. Solé, J. Massons, A. Speguini, M. Bettinelli, C. Cascales, M. Aguiló, F. Díaz, *Phys. Chem. Chem. Phys.* 2014, **16**, 1679-1686.

20 T.Li, C. Guo, P. Zhao, L. Li, J.H. Jeong, *J. Am. Chem. Soc.* 2013, **96**, 1193-1197.

21 R. Calderón-Villajos, C. Zaldo, C. Cascales, *Nanotechnology* 2012, **23**, 505205.

22 A. Stockman, D. I. A. MacLeod, N. E. Johnson, *J. Opt. Soc. Am. A* 1993, **10**, 2491-2521.

23 S. Kück, A. Diening, E. Heumann, E. Mix, T. Sandrock, K. Sebald, G. Huber, *J. Alloys Comp.* 2000, **300-301**, 65-70.

24 G. Özen, O. Forte, B. DiBartolo, J. M. Collins, *J. Appl. Phys.* **2007**, **102**, 023110.

25 G. S. Maciel, R. B. Guimaraes, P. G. Barreto, I. C. S. Carvalho, N. Rakov, *Opt. Mater.* 2009, **31**, 1735-1740.

26 R. Naccache, F. Vetrone, A. Speghini, M. Bettinelli, J. A. Capobianco, *J. Phys. Chem. C* 2008, 112, 7750-7756.

27 K. Lemański, P. J. Dereń, *J. Luminesc.* 2014, **146**, 239-242.

28 L. Aarts, B. M. van der Ende, A. Meijerink, *J. Appl. Phys.* 2009, **106**, 023522

29 E. N. Silva, A. P. Ayala, J. Y. Gesland, R. L. Moreira, *Vib. Spectrosc*. 2005, **37**, 21-26.

30 M. M. Lage, A. Righi, F. M. Matinaga, J. Y. Gesland, R. L. Moreira, *J. Phys. Condens. Matter* 2004, **16**, 3207-3218

31 M. C. Nostrand, R. H. Page, S. A. Payne, L. I. Isaenko, A. P. Yelisseyev, *J. Opt. Soc. Am. B* 2001, **18**, 264-276.

32 D. J. M. Bevan, J. Mohyla, B. F. Hoskins, R. J. Steen, *Eur. J. Sol. State. Inorg. Chem.* 1990, **27**, 451-465.

33 T. Passuello, F. Piccinelli, M. Trevisani, M. Giarola, G. Mariotto, L. Marciniak, D. Hreniak, M. Guzik, M. Fasoli, A. Vedda, V. Jary, M. Nikl, V. Causin, M. Bettinelli, A. Speghini, *J. Mater. Chem.* 2012, **22**, 10639-10639.

34 K. I. Schaffers, W. F. Krupke, W. K. Bischel, S. A. Payne, J. B. Tassano, P. A. Waide, R. H. Page, *J. Opt. Soc. Am. B* 1998, **15**, 996-1008.

35 S. Zhou, K. Deng, X. Wei, G. Jiang, C. Duan, Y. Chen, M. Yin, *Opt. Commun*. 2013, **291**, 138-142.

36 Joint Committee on Powder Diffraction Stardards-International Center for Diffraction Data, www.icdd.com.

37 T. Smith, J. Guild, The C.I.E. colorimetrics standards and their use, Trans. Opt. Soc. 1931**,** **33**, 73-134. Commission Internationale de l'Eclairage Proceedings, Cambridge University Press, Cambridge, UK, 1931.

38 S. Burikov, T. Dolenko, S. Patsaeva, Y. Starokurov, V. Yuzhakov, *Mol. Phys.* 2010, **108**, 2427-2436.

[39] M.E. Spahr, P.B. Bitterli, R. Nesper, M. Muller, F. Krumeich, H.V. Nissen, *Angew. Chem. Int. Ed*. 1998, **37**, 1263.

[40] X. Wang, X. Sun, D. Yu, B. Zou, Y. Li, **Adv. Mater.** 2003, **15**, 1442-1445.

41 C. Cascales, C. Zaldo, F. Esteban-Betegón, R. Calderón-Villajos, *CrystEngComm* 2012, **14**, 3577-3579.

42 R. Calderón-Villajos, C. Zaldo, C. Cascales, *CrystEngComm* 2012, **14**, 2756-2768.

43 F. Vetrone, J. C. Boyer, J. A. Capobianco, A. Speghini, M. Bettinelli, *J. Phys. Chem. B*, 2003, **107**, 1107-1112.

44 E. W. Barrera, M. C. Pujol, F. Díaz, S. B. Choi, F. Rotermund, K. H. Park, M. S. Jeong, C. Cascales, *Nanotechnology*, 2011, **22**, 075205.

45 C. Zaldo, M. Rico, C. Cascales, M. C. Pujol, J. Massons, M. Aguiló, F. Díaz, P. Porcher, *J. Phys.Condens. Matter* 2000, **12**, 8531-8550.

46 C. Cascales, C. Zaldo, *Chem. Mater.* 2006, **18**, 3742-3753.

47 R. Balda, J. Fernández, A. Mendioroz, M. Voda, M. Al-Saleh, *Phys. Rev. B*. 2003, **68**, 165101.

48 A. Mendez-Blas, M. Rico, V. Volkov, C. Cascales, C. Zaldo, C. Coya, A. Kling, L. C. Alves, *J. Phys. Condens. Matter* 2004, **16**, 2139-2160.

49 M. P. Hehlen, H. Riesen H. U. Güdel, *Inorg. Chem.* 1991, **30**, 2273-2277.

50 T. R. Gosnell, *Electron. Lett.* 1997, **33**, 411-413.

51 M. J. Weber, *J. Chem. Phys.* 1968, **48**, 4774-4780.

52 F. Pellé, M. Dhaouadi, L. Michely, P. Aschehoug, A. Toncelli, S. Veronese, M. Tonelli, *Phys. Chem. Chem. Phys*. 2011, **13**, 17453-17460.

53 C. de Mello Donegá, A. Meijerink, G. Blasse, *J. Phys. Chem. Solids* 1995, **56**, 673-685.

54 E. G. Reut, A. I. Ryskin, *Phys. Status Solidi A* 1973, **17**, 47-57.

55 L. H. Acioli, A. S. L. Gomes, C. B. de Araújo, C. N. Ironside, *Phys. Rev. B* 1996, **54**, 9126-9130